FRICTIONAL PROPERTIES OF 2D HYBRID ORGANIC-INORGANIC PEROVSKITES

A Thesis

by

RAJ SANJAYKUMAR PATEL

Submitted to the Graduate and Professional School of
Texas A&M University
in partial fulfillment of the requirements for the degree of

MASTER OF SCIENCE

Chair of Committee,	Qing Tu
Co-Chair of Committee,	Kelvin Xie
Committee Members,	Jonathan Felts
Head of Department,	Ibrahim Karaman

August 2021

Major Subject: Materials Science and Engineering

ABSTRACT

Two-dimensional (2D) hybrid organic–inorganic perovskites (HOIP) possess high chemical stability, low production cost, and great optoelectronic and semiconductor properties, which permit great potential in widespread applications such as solar cells, light emitting diodes, flexible devices and triboelectric nanogenerators (TENGs). During these applications, 2D HOIPs would slide against each other or other interfacing materials causing damage or changes to the structure of HOIPs during service. Understanding the frictional properties of 2D HOIPs are thus vital for the durability and performance of these devices. However, little is known about the frictional behaviors of 2D HOIPs. Main objectives of this work are to shed light on the effect of organic ligands and humidity on the friction behavior of HOIPs. In this work, Friction coefficients of two most commonly used single crystalline HOIPs, butylammonium lead iodide ($(BA)_2PbI_4$ (C4n1)) and phenylethyl ammonium lead iodide ($(PEA)_2PbI_4$ (PEAn1)), are measured under different humidity conditions using Friction force microscopy with a diamond coated probe. The COF of PEAn1 is found always lower than that from C4n1 in both ambient and dry environments, probably due to the higher hardness of PEAn1 and the steric hinderance of phenyl terminal group preventing direct interaction of the tip with underlying methylene groups. The humidity shows different effects on the COFs of the AFM tip sliding on the two HOIP crystal surfaces. The difference might be related to the hydrophobicity of the spacer molecules, the moisture-induced packing of the organic ligands on the surfaces, and the non-monotonic dependence of COF on the amount of water molecules at the tip-

sample interface. The thesis concludes with a discussion on future research directions related to the frictional properties of 2D HOIPs.

DEDICATION

To My Mom and Dad

ACKNOWLEDGEMENTS

I would like to thank my committee chair, Dr. Qing Tu, and my committee members, Dr. Kelvin Xie, Dr. Jonathan Felts, for their guidance and support throughout the course of this research.

Thanks also go to my friends and the department faculty and staff for making my time at Texas A&M University a great experience.

Finally, thanks to my mother and father for their encouragement and love.

CONTRIBUTORS AND FUNDING SOURCES

Contributors

This work was supervised by a thesis committee consisting of Professor Dr. Qing Tu and Dr. Kelvin Xie of the Department of Material Science and Engineering Department and Professor Dr. Jonathan Felts of the Department of Mechanical Engineering Department. 2D HOIPs provided were synthesized by Dr. Ioannis D. Spanopoulos from Northwestern university.

All other work conducted for the thesis was completed by the student independently.

Funding Sources

Graduate student was supported by Dr. Qing Tu

NOMENCLATURE

2D HOIPs	Two-Dimension Hybrid Organic Inorganic Perovskites
TENGs	Triboelectric Nano-generators
PV	Photo-voltaic
SAMs	Self-assembled Monolayers
RH	Relative Humidity
C4n1	Butylammonium Lead Iodide ($(BA)_2PbI_4$)
PEAn1	Phenylethyl Ammonium Lead Iodide ($(PEA)_2PbI_4$)
UV	Ultraviolet
BA	Butylammonium
PEA	Phenylethyl Ammonium
AFM	Atomic Friction Microscope
FFM	Friction force Microscopy
ITO	Indium Tin Oxide
COF	Co-efficient of Friction
δ	Deflection Sensitivity (nm/V)
Δ	offset Signal (V)
kn	Normal Spring Constant (nN/nm)
s	Set Point Voltage (V)
S	Shear Strength
H	Hardness

N	Normal Force (nN)
W	Lateral Signal (V)
W’	Lateral Prime Signal (V/nN)
Δ’	Offset Prime Signal (V/nN)
α	Lateral Force Constant (nN/V)
μ	Friction Co-efficient
L	Lateral Force (nN)

TABLE OF CONTENTS

Page

LIST OF FIGURES

Page

LIST OF TABLES

Page

CHAPTER I

INTRODUCTION

Hybrid organic-inorganic perovskites

Perovskites (e.g., $CaTiO_3$, $LaAlO_3$, $MgSiO_3$) have a general formula of AMX_3, where M and X atoms will form a $[MX_6]^{-4}$ octahedral structure and A-cations sit in the cavities among the octahedra (Figure 1). Hybrid organic-inorganic perovskites (HOIPs) are an emerging family of semiconductor materials where A is usually small organic cations (methylammonium, Cs or formamidinium), M is group 14 divalent metal cations (e.g., Pb^{2+}, or Sn^{2+}) and X is halide anions (I^-, Br^-, Cl^-). 3D HOIPs have attracted substantial research attentions in the past decade as promising materials for optoelectronic applications due to their excellent properties, including large absorption coefficient[1], long carrier diffusion length[2-4], small effective masses for electrons and holes, dominant point defects that only generate shallow levels, and grain boundaries that are essentially benign, as well as high photo-luminescence and photovoltaic efficiencies[3, 5]. The above-mentioned properties in combination with HOIPs' scalable solution-based production and compositional flexibility, HOIPs are ideal active materials for high-efficiency solar cells, light-emitting diodes, photodetectors, and semiconductor lasers with different values of properties by changing between different structural chemistry.[6, 7] Furthermore, HOIPs are relatively soft compared to their oxide analogs,[8-10] which enables HOIPs' application in some wearable and flexible devices such as soft photodetectors, flexible triboelectric nanogenerators.[11-16]

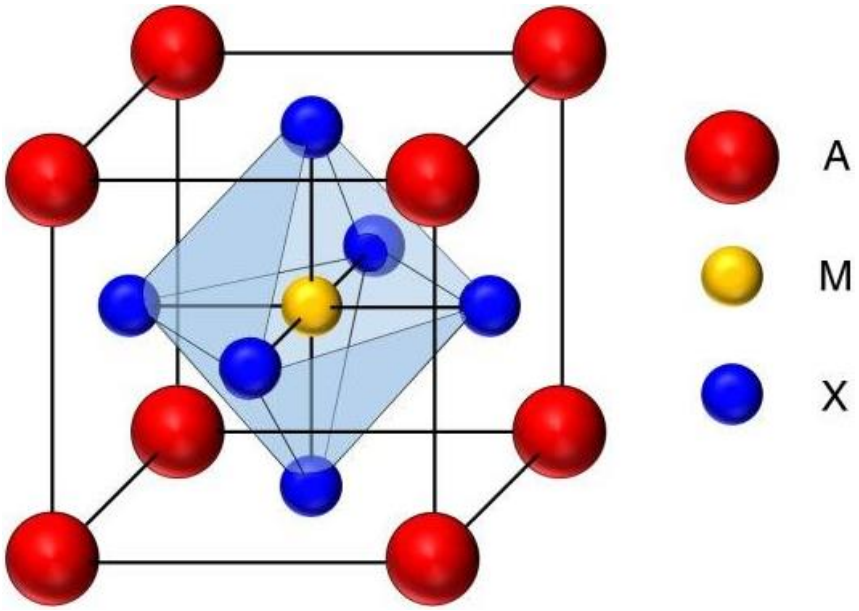

Figure 1 Perovskite generic lattice structure with AMX_3, the blue cage represents $[MX_6]^{-4}$.[17]

However, 3D HOIPs suffer from chemical stability issues where humidity, oxygen and ultraviolet (UV) light can degrade the materials over a short period of time, which significantly impedes their commercial viability.[18, 19] As such 2D HOIPs are implemented in recent development of advance devices owing to much higher stability and other improved properties compare to their 3D counterparts.[20-23] 2D HOIPs have general formula of A_2MX_4 2D HOIPs have 4 neighbors $[MX_6]^{-4}$ octahedra within a single plane against 6 neighbor octahedrons in 3D counterparts as seen in Figure 2. They can be structurally derived from 3D HOIPs by partially remove the $[MX_6]^{-4}$ octahedra along certain crystallographic directions, and insert organic spacer molecules, resulting an alternating organic-inorganic structure (Figure 2). Each repeat unit in 2D HOIPs will

interface each other through the weak van der Waals (vdW) interface between the organic spacer molecules.

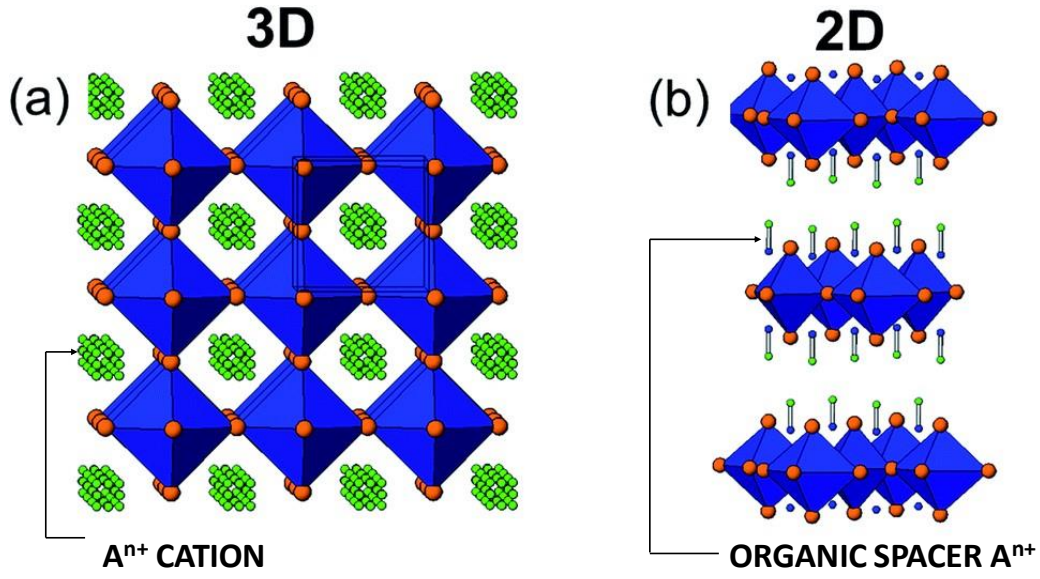

Figure 2 Crystal structure of (a) 3D and (b) 2D HOIPs showing the difference in structure due to different type of organic cation arrangement.[24]

Owing to the presence of hydrophobic spacer molecules, 2D HOIPs can resist the moisture attack much better than the 3D HOIPs, and exhibit significantly improved stability. The current state-of-the-art HOIP-based solar cells with a record stability involves 2D HOIPs and has been demonstrated with a life time of years, greatly promoting the commercial viability of HOIP photovoltaics.[20, 24-27] Furthermore, the 2D structure significantly relaxed the size constraints on the organic cations outlined by the Goldschmidt rule[28], which allows for an almost unlimited option to engineer the structure and physical properties of 2D HOIPs, including mechanical, thermal and electronic properties. Currently, there are over 50 different organic cations that have been

incorporated into 2D HOIPs, with various combination of the inorganic metal halide framework.[29-31] Among the vast options of ammonium organics spacer molecules, linear alkyl chain with methane or aromatic end functional groups are most widely used, particularly butylammonium (BA) and phenylethyl ammonium (PEA).

Current Understanding of the Mechanical Properties of HOIPs

Mechanical strains are ubiquitously encountered by HOIPs during device fabrication and application, especially for devices in flexible form factors.[8, 32-34] The mechanical strain can lead to stability issues such as fracture, shear sliding, wear and delamination, which are equally important to the durability of devices as the chemical stability of the functional materials.[34-36] Hence it is vital to understand the mechanical properties of HOIPs and their relationship to the chemical compositions and structures. The elastic mechanical properties of 3D HOIPs, such as Young's modulus, Poisson's ratio, shear modulus and bulk modulus, have been investigated by experiments and computational simulations.[32, 37-40] These properties are found to be mainly determined by the metal-halide bonding strength, with a limited but not negligible influence from the organic cations.[37-40] The Young's moduli of 3D HOIPs are found to be in 10 – 30 GPa range, softer than other inorganic oxide perovskites (e.g., $BaTiO_3$) or inorganic photovoltaic materials (e.g., Si, or CdTe),[41-45] owing to the large deformability of the octahedra and the organic component in the materials. Such soft structure gives little resistance during phase transition, ion migration and can also promote self-healing of material.[29, 46-48]

The structure softness together with the combination of good semiconductor properties enables the application of HOIPs into flexible electronics.[8, 9, 23, 34]

Study on the mechanical properties of 2D HOIPs has just emerged recently. Instrument nanoindentation was implemented to measure the young's modulus and hardness of 2D HOIPs in the out-of-plane directions. Compared to their 3D analogs, 2D HOIPs are even softer due to the presence of soft organic spacer and the weak vdW interactions.[49] Increasing the relative fraction of the organic component in the crystal structure by controlling the length of the linear alkylammonium spacer molecules from 4 carbon 12 carbons first further soften the 2D structure, and then the softening effect will eventually saturate because the enhanced inter-chain vdW interaction associated with the increased chain length will compensate for the weakening effect.[49] Besides the thickness of the organic layer, the interface between the organic layer and the deformability of the organic layer can also influence the resulting out-of-plane mechanical properties.[49] For instance, incorporating spacer molecules with highly deformable ring structure than rigid benzene will give a softer 2D HOIP.[10] Furthermore, spacer molecules with stronger interlayer interaction (e.g., $\pi - \pi$ interaction) will lead to higher elastic modulus.[10] In addition to the out-of-plane mechanical properties, in-plane mechanical properties (Young's modulus and breaking strength) were reported by AFM stretching of suspended ultrathin 2D HOIP membranes.[34, 49] Monolayer (i.e., single repeat unit) 2D HOIPs exhibits an elastic modulus very similar to their 3D counterparts because the vdW interface is absent in monolayer case and the inorganic octahedral framework is dominating the mechanical behavior of the flake, which has a structure very similar to those in 3D HOIPs. However,

as the thickness increases to bilayer or thicker, both the young's modulus and breaking strength decrease and then plateau around 3 layers, similar to many other 2D materials. This suggests that the 2D layers slide against each other during the mechanical deformation, which indicate that controlling the interfacial interaction through the organic spacer molecules could tune the in-plane mechanical properties of 2D HOIPs.[34]

Recently, HOIPs are employed in triboelectric nanogenerators (TENGs), which result in a considerable yield in triboelectric charges due to its remarkable dielectric features which helps in maintaining charges for longer time.[50-52] TENGs are devices that convert small mechanical vibration energy to electric power.[53-57] Their operating principle relies on conjunction of triboelectrification and electrostatic induction between two triboelectric materials.[12, 54-57] New concepts of self-powered HOIP photodetectors where the triboelectric and optoelectronic properties of hybrid perovskites were utilized to achieve the functionality.[16, 58] However, the resistance of HOIPs to mechanical damage is rather poor.[59-61] This can be particularly crucial for TENG applications, in which the HOIP layer is constantly moving against other materials and can experience significant wear. The frictional properties of HOIPs are thus vital for the longevity of the HOIP-based devices. Yet little is known about the frictional properties of HOIPs.

Bi et al.[62] first studied the friction coefficient (COF) between $(BA)_2PbBr_4$ and indium tin oxide ITO (a widely used transparent electrode for solar cell applications) using AFM. 2D $(BA)_2PbBr_4$ HOIP flakes were drop casted onto an ITO (111) substrate and were capped with SiO_2 to ensure a uniform loading during friction test. An AFM tip is placed

at the center of the square flake to apply a normal load. Then the AFM tip will be utilized to drive the sliding at the 2D HOIP-ITO interfaces to measure the frictional force and COF along different directions. The 2D HOIP-ITO interfaces exhibit anisotropic friction behavior with 4-fold-symmetry. The COF (μ) varies from 0.015 in aligned contacts to 0.035 in mis-aligned contacts, which is caused by moiré-induced lattice distortion. Interestingly, the frictional anisotropy decreases monotonically with the thickness of the membrane, and becomes negligible when it is more than 16 layers. Furthermore, in ambient environment, moisture is present at different levels and might fluctuate over time. It might affect the packing of the spacer molecules and thus their interactions with interfacing materials. Yet, little is known how the humidity will affect the frictional properties of 2D HOIPs.

Frictional Properties of Similar 2D materials and Self-Assembled Monolayers

Self-assembled monolayer (SAM) is a single molecule thick layer of material which bonds to a surface via physical or chemical forces during deposition process. 2D HOIPs can be viewed as two SAMs sandwiching a metal halide octahedral layer. Hence, existing knowledge on SAMs' frictional properties can help us understand the friction behavior of HOIPs. Sung, et al.[63] measured COF for alkyl terminal group with $CH_3(CH_2)_{15}SH$ SAMs on a gold substrate using Si_3N_4 tip in AFM, where value of friction is found to be 0.06. Similarly, Lee, et al.[64] found the friction of 0.015 along different direction for $C_6H_5(CH_2)_{14}SH$ phenyl terminal group SAMs on gold using Si_3N_4 probe. From the friction behavior of SAMs, the methane terminal groups seem to have higher COF than phenyl

groups. According to Lee, the friction friction properties were higher for the SAMs with methane terminal group is because of increased vdW interaction due to the exposed underlying methylene groups to the AFM tip, which is not the case in the phenyl-terminal SAMs due to steric blocking of underlying methylene group by the large overlying terminal group.[64] Tian, et al.[65] and Qian, et al.[66] measured friction behavior of octadecyltriethoxysilane (OTE) and for $CH_3(CH_2)_n SH$ (n = 9, 17) using Si_3N_4 tip in AFM, respectively. According to both papers the effect of humidity is affected by the hydrophobicity of the materials used. Generally speaking, for relative humidity (RH) below 40%, raising RH can significantly increase the friction, because the adsorbed water increases the adhesion between tip and sample, causing an increase in friction response of SAMs. However, when RH is over 40%, higher RH leads to lower friction, where the excess water molecules start to act as lubricant between the tip and SAM surface.

Highly ordered pyrolytic graphite (HOPG) is another 2D crystal similar to 2D HOIPs, i.e., strong in-plane bonds (covalent or ionic) but weak interlayer bonds (vdW bonds). The COF between HOPG and a diamond-like carbon tip measured by friction force microscopy is about 0.125 ± 0.06, while other tip materials (e.g., Si or Si_3N_4) gives much lower COFs.[67] Another study of the friction properties of HOPG showing anisotropic friction behavior with respect to the basal plane of HOPG. In this work, COF between a copper alloy ($Cu_5Pb_5Zn_5Sn$) and HOPG was found to be around 0.085 using tribometer.[68] This Cu-alloy-HOPG COF did not change notably for changing the normal force and scanning speed.[68] Furthermore, at 40% RH, the friction is found to be lower in nitrogen environment compare to that in air.[68]

Friction behavior of MoS_2, is studied to understand the effect of humidity on friction properties. Using 100 nm MoS_2 coated SiN_3 tip, the COF for single crystal MoS_2 is ultra-low (0.012 ± 0.002) compare to 200 nm polycrystal MoS_2 coating (0.41 ± 0.05) on single crystal silicon surface with oxide layer.[69] The study also shows that humidity has no effect on COF of single crystal MoS_2 as both the tip surface and sample surface are hydrophobic in nature contrast to the water molecules at edges of polycrystal MoS_2.[69] Furthermore, friction force microscopy finds that the friction between a SiN_3 tip and a MoS_2 single crystal along basal plane increases as a function of RH.[70] But the adhesion force is not affected by change in humidity, suggesting that water directly alter the tip-MoS_2 interfacial shear strength rather than indirectly through working as capillary condensation on tip.[70]

Friction Force Microscopy

Frictional force microscopy is a widely used technique to characterize the frictional properties of advanced functional materials.[63, 67, 69] In FFM, the lateral distortion of the AFM cantilever due to the frictional force between the sample surface and AFM probe during the scan is detected through a photodiode as seen in Figure 3.

By calibrating the photodiode and the AFM cantilever, the frictional force and applied normal force between the AFM tip and the material surface can be quantified.[12] Studying the frictional force from the AFM scan aid us in comprehending the friction behavior of material[71]. It also assists us in detecting the adhesion force, wear limit, wear volume for certain pressure, damage due to friction and calculating material loss.[72, 73]

FFM has been extensively employed to investigate the friction behavior of 2D materials (*e.g.*, graphene and MoS_2) and self-assembled monolayers.[63, 67, 69] Furthermore, FFM helps in understanding the mechanism at the interface between the contact surface of materials, which is critical for future development of advance devices that implement 2D multi-functional materials.

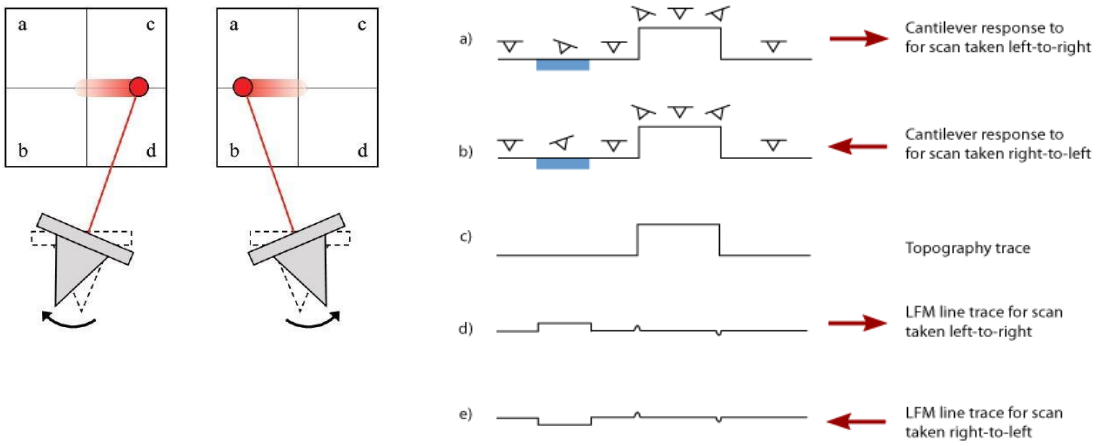

Figure 3 Left- this way the lateral deflection is detected by the photodiode. Right- Change in Lateral deflection profile due to different COF material and height variation.[74]

Objective of this work

While the frictional properties of 2D HOIPs are crucial for the mechanical reliability of the HOIP devices and the performance of HOIP-based TENG applications, their frictional behavior largely remains unknown. Here, I measure the COF of 2D HOIPs with a general formula of $(R\text{-}NH_3)_2PbI_4$ by FFM to address the following two fundamental questions: 1) How will the end functional group affect the frictional properties of $(R\text{-}NH_3)_2PbI_4$ 2D HOIPs? 2) How will the humidity affect the frictional properties of (R-

$NH_3)_2PbI_4$ 2D HOIPs? I will focus on two presentative examples of the most popular linear alkylammonium and aromatic spacer molecule families, *i.e.*, $CH_3(CH_2)_3NH_3$ (BA) and $C_6H_5(CH_2)_2NH_3$ (PEA). Specifically, I measure the COF for $(BA)_2PbI_4$ (C4n1) and $(PEA)_2PbI_4$ **(**PEAn1) using diamond coated tip in AFM in ambient condition as well as in low humidity environment. The research work sheds light on the frictional behavior of 2D lead-iodide HOIPs and the influences of organic spacer molecules and environmental humidity on the materials' tribological properties, providing valuable insights into improve the mechanical stability of 2D HOIPs involving friction.

CHAPTER II

MATERIALS AND METHODS

Materials

$(BA)_2PbI_4$ (C4n1) and $(PEA)_2PbI_4$ (PEAn1) are used for the experiments which were synthesized by Dr. Ioannis D. Spanopoulos from Northwestern University. As mentioned before these two HOIPs are used due to their abundant use compare to other HOIPs. Figure 4 shows the structure for PEAn1 with chemical compound of BA and PEA drawn on the side. C4n1 have the same structure, just changing the organic ligand in between the layers.

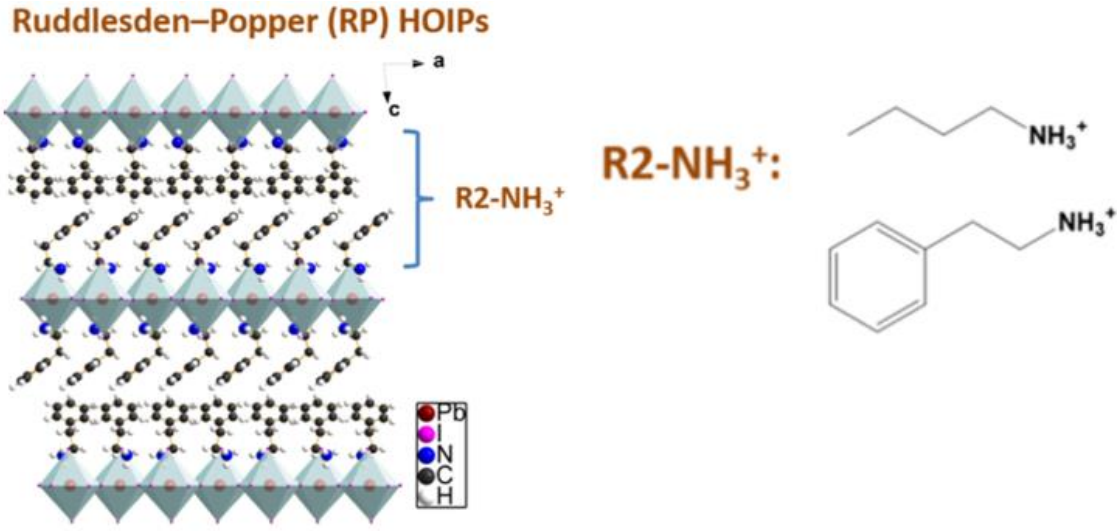

Figure 4 Structure of layered $(PEA)_2PbI_4$ and the different organic ligands used which are BA and PEA.[10]

Synthesis and Characterization

Different amount of PbO powder was dissolved in 57% w/w aqueous HI solution, depending on the HOIP sample to be synthesized, in a glass volumetric flask by heating to boiling under constant magnetic stirring for about 5 min, which formed a bright yellow solution. Then fixed amount of either butylamine or phenethylamine were added, for making C4n1 or PEAn1 respectively, to 50% aqueous H_3PO_2, also of fixed volume, and this solution was added to the reaction slowly. The stirring was then discontinued, and the solution was left to cool to room temperature during which time big orange plate crystals started to crystallize. The crystals were isolated by suction filtration and thoroughly dried under reduced pressure.

The structural characterization for C4n1 and PEAn1 are as shown in Figures 5 and Figure 6 respectively.

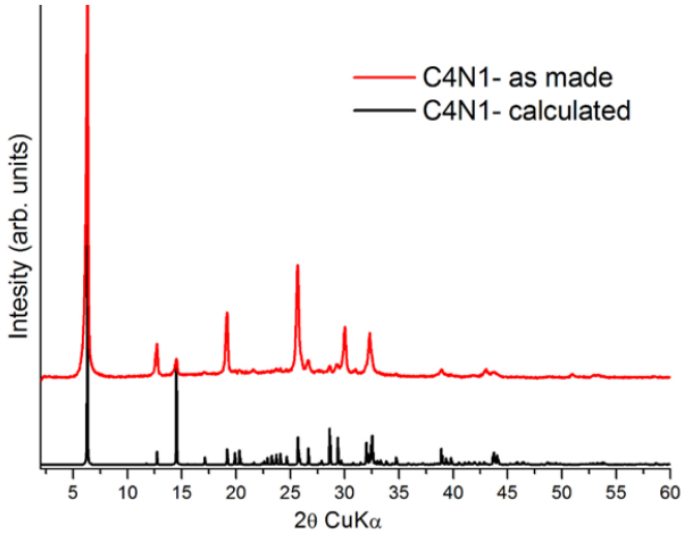

Figure 5 Comparison of the calculated PXRD pattern from the solved single crystal structure of the $(CH_3(CH_2)_3NH_3)_2PbI_4$ (C4n1) material (including preferred orientation (001)) and the experimental determined one from the as made crystals.[10]

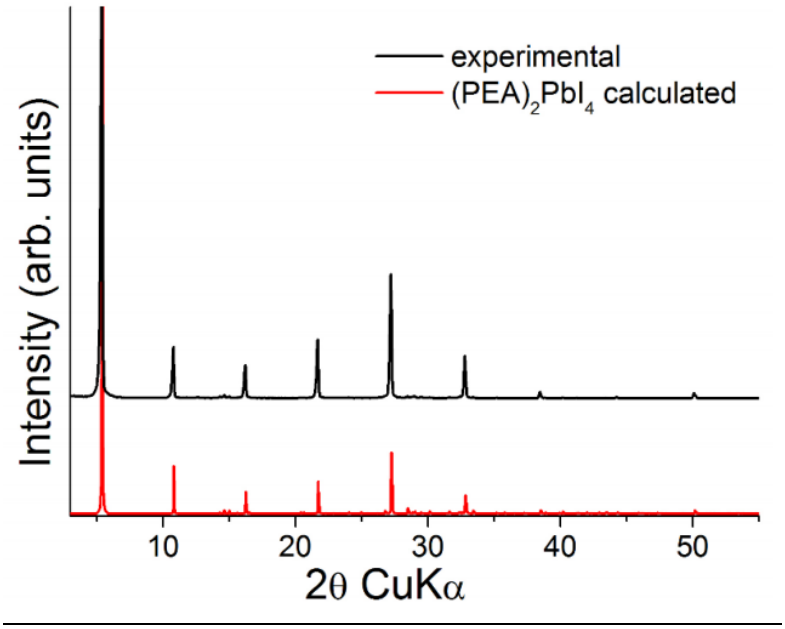

Figure 6 Comparison of the calculated powder X-ray diffraction pattern from the solved single crystal structure of the 2D RP HOIP $(PEA)_2PbI_4$ (PEAn1) material and experimental determined one from the as made crystals.[10]

Sample Preparation

Thick flakes of the single crystal 2D HOIPs were used. A metal disc is used to mount the sample. First, the metal disc is cleaned with ethanol to remove any contamination from the surface of the metal. The perovskite flake sample is then glued to the substrate using silver paste after which the prepared sample is kept in a dry environment for more than 1 hours to cure the glue. Prior the FFM measurements, the crystal where mechanical exfoliated to reveal fresh surfaces for the study.

Experimental Procedure

FFM is performed on an MFP-3D-Infinity AFM using a diamond coated probe. Here the diamond coated probe is selected because of its strong resistance to wear to reduce the influence of tip wear on the frictional study. FFM measures the frictional force as a function of normal force. Thus, a calibration of the lateral and normal spring constant as well as lateral/normal sensitivity is required. The procedure follows the method developed by *Ogletree, et al.[12]* for friction force calibration in AFM as described below. A micro fabricated Silicon chip, purchased from Nano and More Co., is used with known slope ridges for lateral force calibration.

Normal Force Calibration

The normal deflection sensitivity (δ) (nm/V) of the AFM photodiode is first calibrated by doing a force curve on a silicon wafer cleaned by Piranha solution, a mixture of 3 parts concentrated (98%) sulfuric acid and 1 part 30% hydrogen peroxide. The normal spring constant (k_n) is then calibrated by fitting the first free resonant peak to the simple harmonic oscillator equation to get power spectral density of the thermal noise fluctuations in air as mentioned in thermal noise dynamic method by *Palacio et al.*[75] The measured spring constant is found to be in range of 1.18 to 1.29 nN/nm which is close to the value provided from manufacturer. The normal force N is the found using Equation 1, where s is setpoint voltage (V) applied.

$$N = s \times \delta \times k_n \quad \ldots\ldots\ldots\ldots\ldots\ldots\ldots\ldots (1)$$

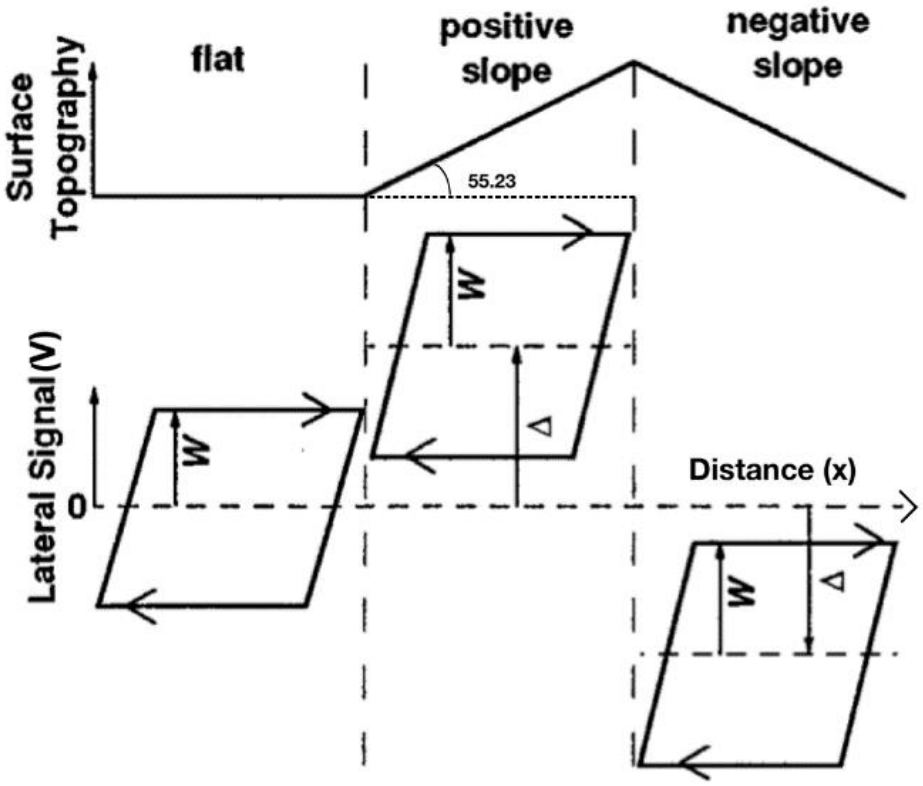

Figure 7 Relation between surface topography and lateral signal. W is lateral force voltage and Δ is offset corresponding to the slope.[12]

Lateral Force Calibration

A micro-fabricated silicon chip having ridges with fixed slope of 55.233˚ and 124.767˚ to the flat surface is used to find the lateral force constant that helps in converting the lateral signal readout from the photodiode (in V) to lateral force (nN) at each normal force used during the scan. For all the Lateral calibrations, a scan length with appropriate flat region and sloped region was selected with the sloped area in the middle of the scan as shown in Figure 8. The speed of the scan (3 μm/s) and the scanned pixels (512 pixels/line)

were kept constant for all the experiments. All the calibration had a set of ten scans with different normal load values. All the load values were kept in the same range (10 – 210 nN). Half the width value between the trace and retrace of sloped surface gives us lateral force signal (W) (V) (Figure 7). Also, the difference between the mean for flat surface and sloped surface will give the offset value Δ (V) as shown in Figure 7. After plotting the W and Δ with respect to normal load, the corresponding slope, W' and Δ' (V/nN), are found which will be independent of the normal force. The COF can then be obtained using Equation 2. After that, the lateral force constant α (nN/V) is calculated using the Equation 3. Lateral force constant can be used to convert the lateral signal scanned for sample to lateral force (L) (nN) using Equation 4.

$$\mu + \frac{1}{\mu} = \frac{2\Delta'}{W' \sin 2\theta} \quad \ldots\ldots\ldots\ldots\ldots\ldots\ldots\ldots \quad (2)$$

$$\alpha W' = \frac{\mu}{\cos^2\theta - \mu^2 \sin^2\theta} \quad \ldots\ldots\ldots\ldots\ldots\ldots \quad (3)$$

$$L = W \times \alpha \quad \ldots\ldots\ldots\ldots\ldots\ldots\ldots\ldots\ldots\ldots \quad (4)$$

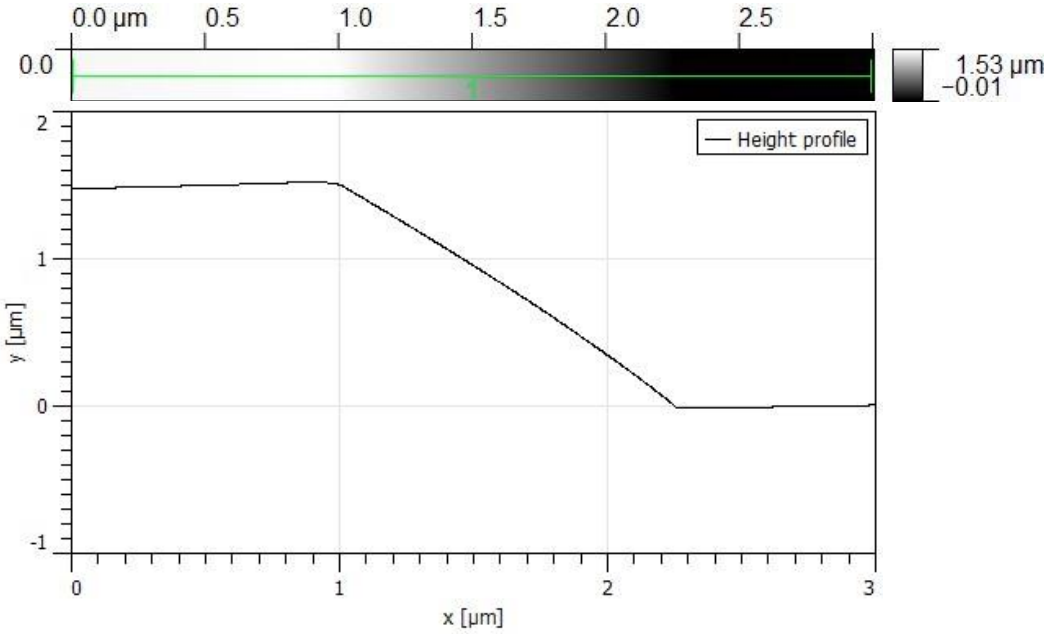

Figure 8 Lateral scan region (top) with Height profile (bottom) for the corresponding section line shown in the lateral scan region.

Lateral Scan of HOIP Sample

After calibrating the AFM cantilever, a flat surface on the sample is selected after scanning a large area, and is scanned with 5 different normal loads ranging from 10 to 110 nN. All the scanning parameters were kept the same as for normal force calibration except for the speed of the scan which was 1.25 µm/s. Lateral signal (W) on the sample will be found for different normal load values and W' will be calculated from the slope of W with respect to normal load which will give us the COF (µ) value between the tip and the contact sample using Equation 5.

$$\mu = W' \times \alpha \quad \ldots\ldots\ldots\ldots\ldots\ldots\ldots\ldots\ldots\ldots \quad (5)$$

As mentioned before two types of samples are employed for the experiments i.e., C4n1 and PEAn1 samples. 36 sets of frictional tests were conducted on at least 3 different single crystals for each type of 2D HOIPs in each testing condition. The histogram of the obtained COF values is fitted to Gaussian distribution.

Humidity Control Set-up

The lab humidity in ambient environment is around 50 ± 5%. To control the humidity during lateral scan on AFM, a closed region around the AFM with a cover having a single inlet for dry gas to pass near the AFM scan region is implemented. The humidity near the cantilever region is measured by a hygrometer. The gas is circulated for 15 min to get the humidity around the tip as dry as possible before starting the experiment work. With this environmental control, the humidity can be dropped to below 7%.

CHAPTER III

RESULTS AND DISCUSSION

FFM Lateral Calibration and Measurements

The lateral scan, region as shown in Figure 8, on the silicon fabricated chip will give us a trace and retrace voltage signals at a normal force value. The sloped region is kept in the middle to cover the whole slope with two points for transition between sloped region and horizontal region for getting better data from the scan (Figure 9).

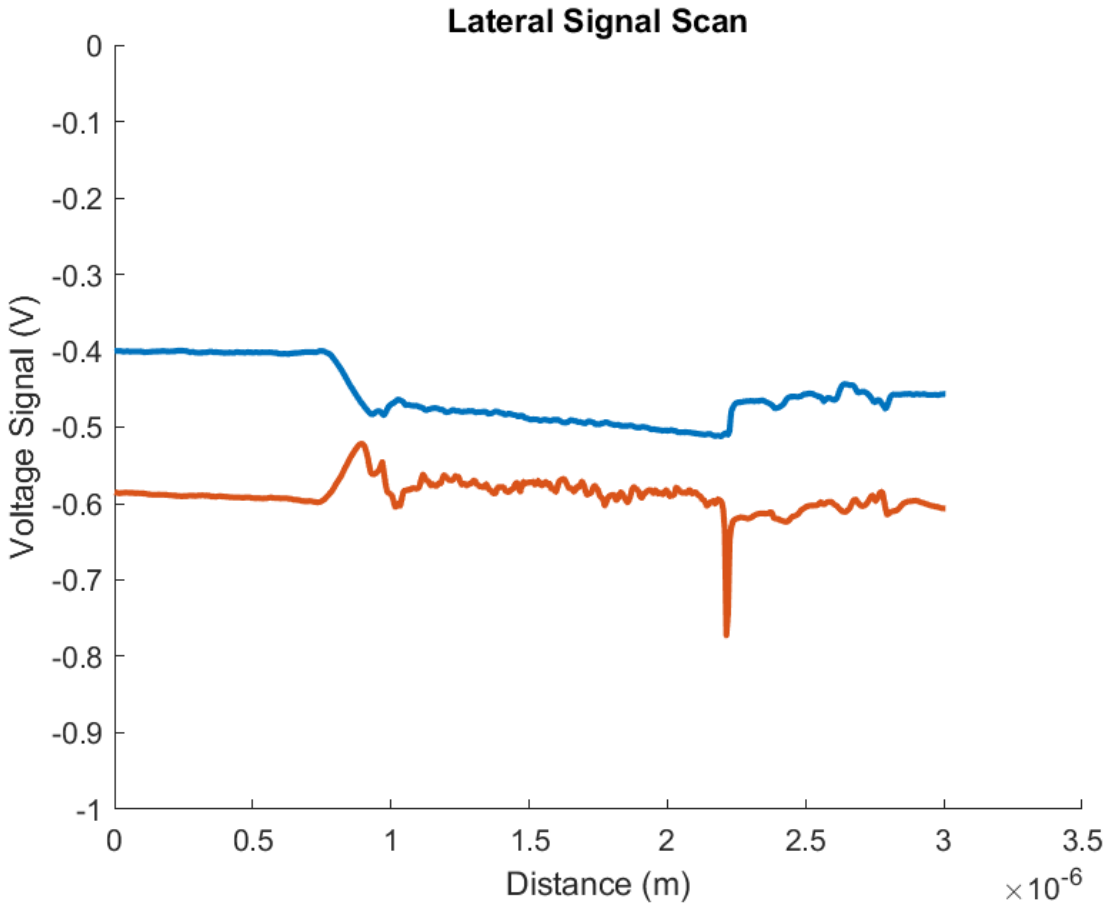

Figure 9 Voltage Signal for trace and retrace with respect to Distance. The middle low signal is for decreasing slope and the high-end parts are flat ridges.

Figure 9 shows a representative lateral trace and retrace scan for 10 nN normal load. The titled region on the curve is when the tip is scanning the slope with an angle of 124.76˚. Without knowing the slope direction, from looking at the trace and retrace voltage signals one can perceive the direction of slope, i.e., if the slope is positive or negative as defined in Figure 7. Figure 9 shows two spikes in the voltage signals showing the transition between the horizontal and the sloped regions. A total of 10 different scans is performed for every lateral calibration with periodically varying normal load. Lateral signal, W, and offset signal, Δ, is calculated for each scan using MATLAB program.

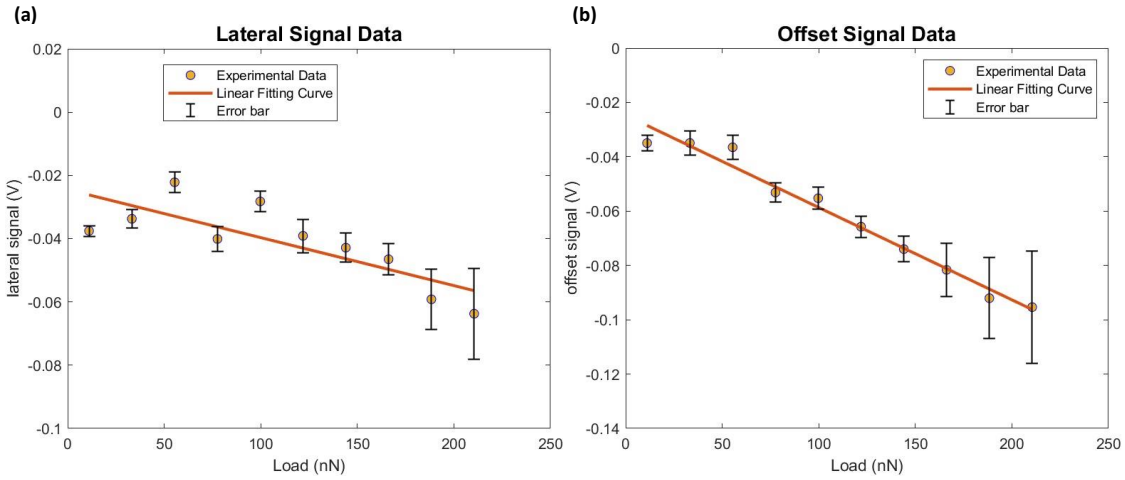

Figure 10 (a) lateral signal for different load values and (b) offset for different load values with error bar and linear curve fit.

After getting the W and Δ value for 10 different normal load values. The slope of W and Δ with respect to the applied normal load, i.e., W' and Δ', can be found by fitting the data to a linear curve (Figure 10). The slope is negative as the retrace signal is subtracted from trace signal. The accuracy of scan decreases for higher normal force as seen in Figure 10 that error bar increases with increasing normal force. Using W' and Δ'

values, the lateral force constant α of the cantilever, and the COF ($\mu_{tip-silicon}$) between the AFM tip and the calibration sample surface are calculated using Equation 2 and Equation 3. α then helps in converting the lateral signal (in the unit of V) to the lateral force (in the unit of N) when measuring the COF between the sample and AFM tip.

As an example, to illustrate the measurement process, a FFM measurement of C4n1 sample in ambient environment is shown here. Bulk sample is used so the surface will be uneven, hence, a large area with scan length of 5 µm is first scanned on the sample to find a smaller area with scan length of 1µm with flat smooth surface to prevent any uneven sloped region during scan. After finding the smooth region as seen in the Figure 11(a), the scan is zoomed to that region, Figure 11(b), and then scanned with different normal load value.

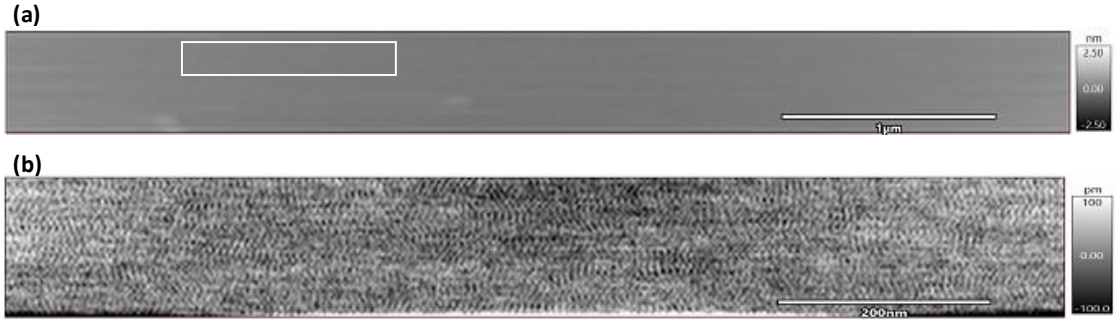

Figure 11 Contact mode AFM topographic image on C4n1 single crystal in ambient environment: (a) 5 µm scan to find the smooth surface and (b) 1 µm scan to find the lateral force signal (W). White box in (a) is the zoomed region.

The smooth sample surface is scanned with 5 different normal loads within a 10 to 110 nN range. W signal at each normal load is extracted and used to calculate lateral force using Equation 4, where the calibrated α for the AFM cantilever is used. Figure 12 shows a representative experimental data of lateral force with respect to normal load on C4n1

sample in ambient environment with linear curve fitting. The lateral force error bar is very small showing that accuracy does not change for different normal force. COF is the slope of the linear fitting curve on the graph of lateral force.

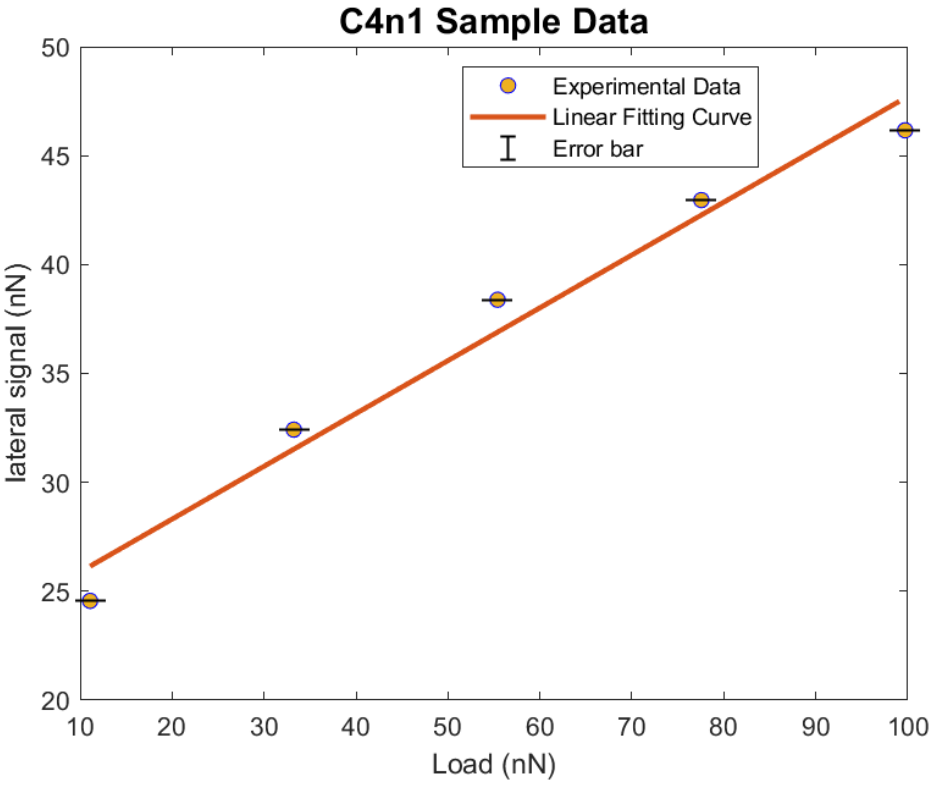

Figure 12 Lateral force vs. normal load from a representative FFM test on C4n1 in ambient environment.

COF of HOIPs

In Ambient Environment

Histogram of the experimentally measured COF of C4n1 in ambient environment is plot in Figure 13 and fitted to Gaussian distribution. The COF is found to be 0.225 ± 0.112 in ambient environment. Although both sharing the same 2D spacer molecules (i.e., BA),

the obtained COF here for C4n1 is much higher than those reported in $(BA)_2PbBr_4$, where the friction between the 2D flake and the ITO substrate is about 0.015 to 0.035[62]. In my experiment, the friction between the AFM tip and the underlying 2D HOIP flakes was measured while in the report in ref. [62], the interface between the 2D flake the ITO is under investigation. The contact geometry (cone-shaped probe vs. planar structure) and interfacing materials (diamond vs. ITO) are significantly different in the two studies. In addition, ref. [62] focuses more on few-layer 2D HOIPs, while my measurements are on bulk 2D HOIP crystals. The difference in the halide species can also influence the packing order of the spacer molecules, which will lead to the variation in friction properties. These differences might have resulted in the measured COF differences.

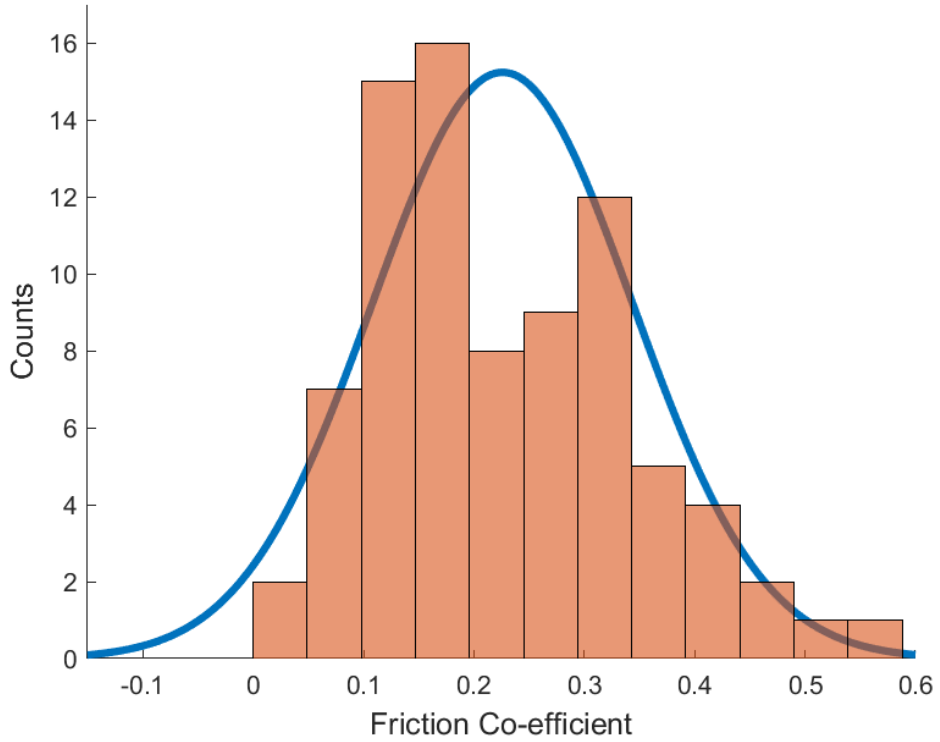

Figure 13 **Experimental test results, showing histogram of COF of C4n1 in ambient environment with solid line representing Gaussian fit of the acquired data.**

Figure 14 shows the measured COF results of PEAn1 samples in ambient condition, where the COF is found to be 0.090 ± 0.041. A Student *t*-test of the COF data from PEAn1 and C4n1 result in a p-value less than 0.05. The results suggest that at 95% confidence, the friction between the diamond-coated probe and the 2D HOIP is significantly lower on PEAn1 than on C4n1, showing the influence of the end functional group of the spacer molecule on the frictional property of 2D HOIPs. This is similar to the frictional behavior found between AFM tip and SAMs, where the COF between the silicon nitride tip and the phenyl terminated SAMs layer on Au is lower than that between the silicon nitride tip and the methane terminated SAM.

The phenyl group is more rigid and thus less deformable than the -CH_3 terminated SAM.[10] PEAn1is also stiffer and harder than C4n1.[10] When the AFM tip is in contact with the 2D HOIPs, the tip will penetrate less into PEA than into BA, resulting less contact, less interaction and thus less friction between the AFM tip and the 2D HOIPs in PEA-based 2D HOIPs than BA-based ones. Furthermore, the phenyl terminal group in PEAn1 work as steric blocking for the AFM tip which prevents increase in vdW interaction of underlying methylene groups resulting in decrease in COF at interface. In contrast, C4n1 does not have large terminal groups in the spacer molecules, which causes easier exposing of the methylene group beneath to the AFM tip during friction test, increasing the vdW interaction between the tip and the organic ligands and hence, increasing friction response at the interface. Thus, the higher stiffness and steric hinderance of PEAn1 than C4n1 results in lower COF on PEAn1.

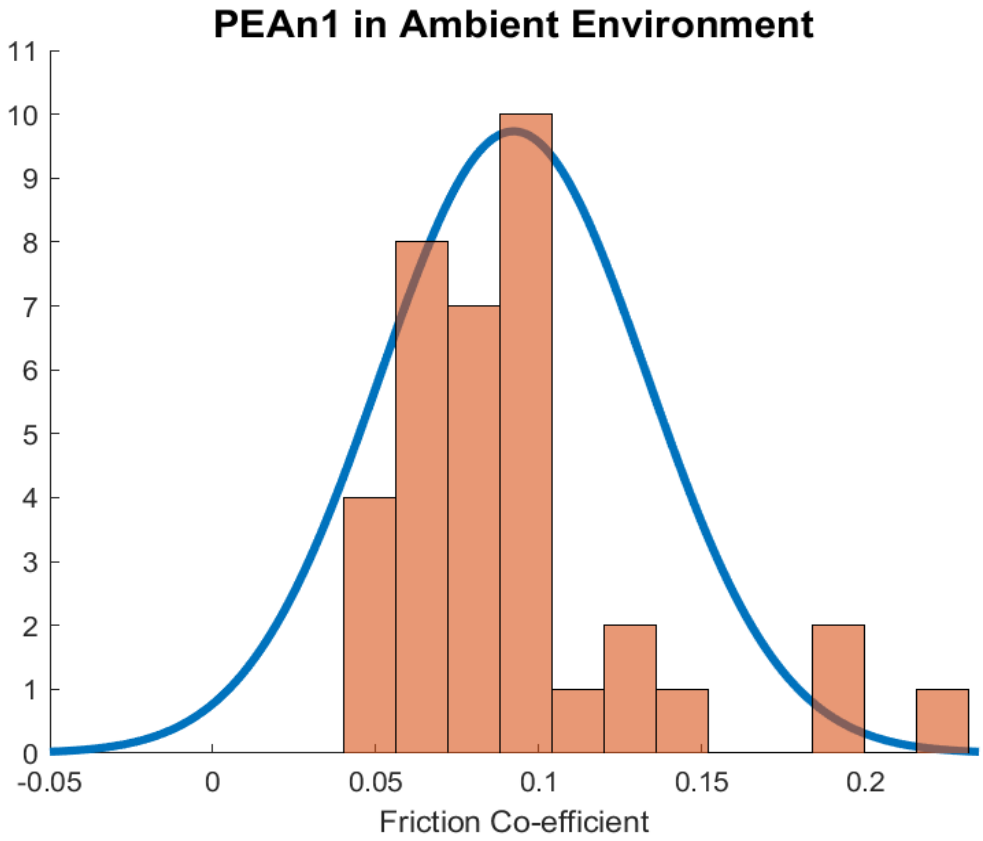

Figure 14 Experimental test results, showing histogram of COF of PEAn1 in ambient environment with solid line representing Gaussian fit of the acquired data.

FFM measured friction HOPG is around 0.1 or less, which is lower than those from C4n1. The stiffer structure in HOPG [10, 68] and the absence of soft organic ligands on the surface might have rendered HOPG with lower COFs. Although the experimental conditions might have contributed to the measured differences in COFs, COF on HOPG is similar to that on PEAn1 in ambient environment[10, 68], where the benzine rings in the phenyl groups are quite similar to the sp2-carbon structure found in HOPG. The COF of single crystal MoS_2 is much lower than those from C4n1 and PEAn1, which might be

because of the additional lubrication effect due to the MoS_2 coating on the AFM tip used in the frictional studies.

In Dry Environment

The same FFM measurements were repeated on the same types of 2D HOIPs, i.e., C4n1 and PEAn1, in dry environment (RH < 7%). C4n1 exhibits an COF value about 0.239 ± 0.066 (Figure 15). The spread of data is reduced slightly compare to data for C4n1 in ambient condition. This might be due to the reduced water meniscus, and moisture-induced packing difference in the spacer molecules, both of which will alter the tip-sample interface in dry environment compared to that in ambient condition. COF of C4n1 is significantly higher in the controlled dry environment than that in ambient condition. However, the difference is not significant (p-value = 0.288).

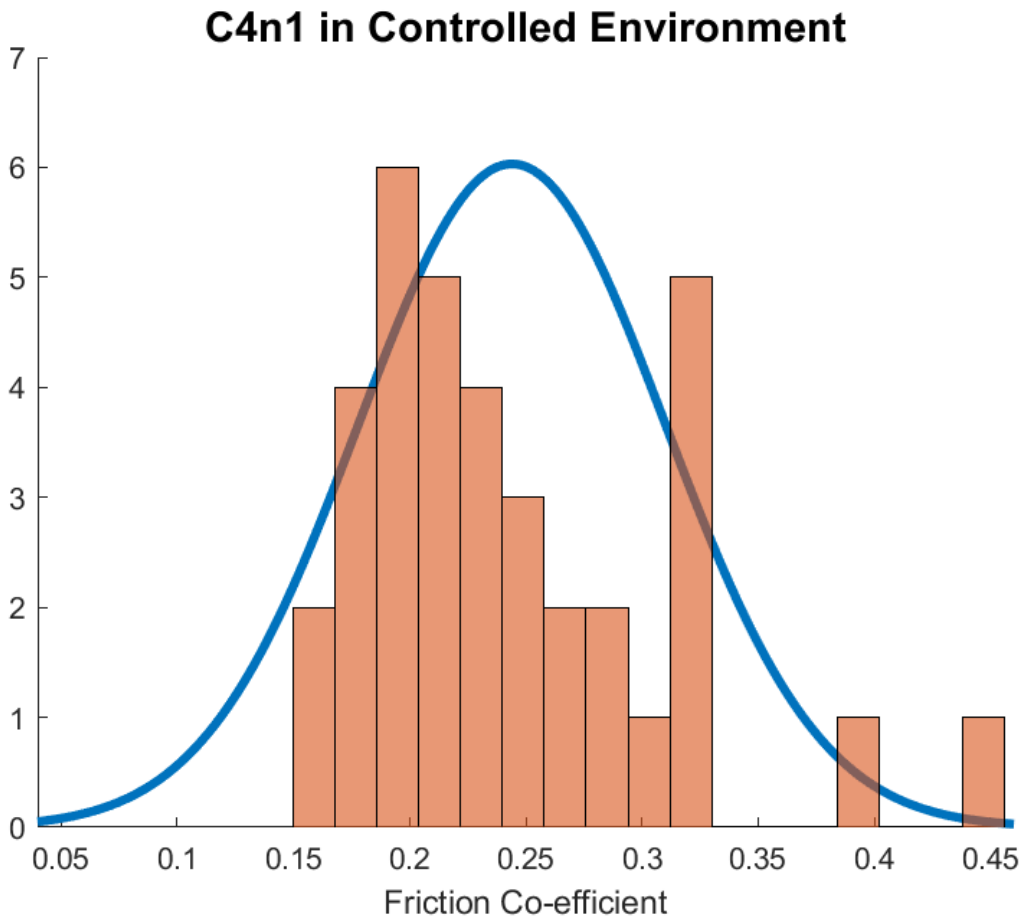

Figure 15 Experimental test results, showing histogram of COF of C4n1 in controlled dry environment with solid line representing gaussian fit of the acquired data.

Figure 16 shows the COF of PEAn1 in dry environment (0.071 ± 0.039). The results show that in dry environment, the PEA-based 2D HOIP still has lower friction than the BA-based counterparts (p-value = 2.7 x 10^{-19}), consistent with the results in ambient conditions. This suggests that although the humidity has an influence on the friction behavior of 2D HOIPs, the COF is probably mainly affected by the end functional group of the spacer molecules. In contrast to the non-significant humidity effect on the COFs on C4n1 2D HOIPs, COF of PEAn1 is significantly lower in the dry environment than

that in ambient conditions (p-value = 0.035), which suggests that end-functional group of the spacer molecule not only affect the interaction between the 2D HOIP surface and the AFM tip, but also the interaction with the water molecules and the 2D HOIP spacer molecules.

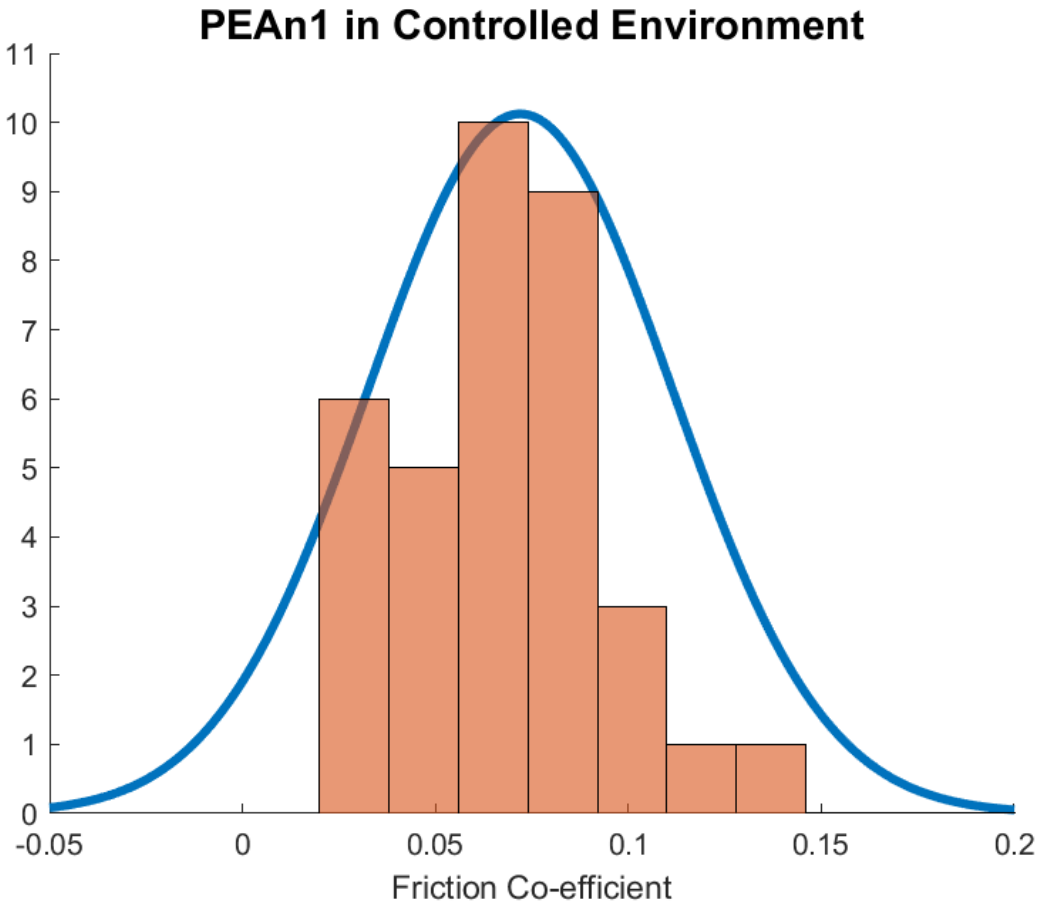

Figure 16 Experimental test results, showing histogram of COF of PEAn1 in controlled dry environment with solid line representing gaussian fit of the acquired data.

According to the studies on the frictional properties of alkyl based SAMs,[65, 66] the effect of humidity on the COF is a non-monotonic function of RH level. Higher RH

induces higher friction between the AFM tip and the SAM when RH is below 40%, but can reduce the COF when RH is above 40%. This is because at relatively low RH (<40%), increasing RH will give rise to stronger adhesion between the tip and the sample materials, causing an enhanced frictional property. Once the RH is above 40%, excess amount of water can present at the tip-sample interface, which can act as lubricant and result in a drop in COF. The overall dependence of COF on the humidity also relies on the hydrophobicity of the sample and tip materials.

Within the tested humidity range, our result suggests that higher humidity cause little or negative impact on the COF values in C4n1, but a significant positive influence on COFs of PEAn1. This might be due to the difference in their hydrophobicity, where the non-polar phenyl group in the PEA spacer molecules renders the material more hydrophobic than the BA spacer molecule. Thus, in ambient environment (50 ± 5% RH), the water meniscus between the tip and the C4n1 HOIP is in excess amount, and the water molecules start to lubricate the interfacial sliding. In contrast, the water meniscus between the tip and PEAn1 is relatively small, and the positive influence of the water molecules on the adhesion contributes to the enhancement of the friction at the tip-PEAn1 interface.

CHAPTER IV

CONCLUSIONS AND FUTURE WORK

Summary of results

In this work, the effects of organic ligands and humidity on friction properties of 2D HOIP single crystals are studied by FFM using a diamond-coated AFM tip. The measured COF values for each type of materials in each environmental conditions are summarized in Table 1.

COF of C4n1 is found higher than PEAn1 both in ambient and in dry environments, similar to results from SAMs with similar terminal functional groups. This is probably due to higher hardness of PEAn1 and the steric hinderance of phenyl terminal group preventing direct interaction of the tip with underlying methylene groups. The humidity shows different effects on the COFs of the AFM tip sliding on the two HOIP crystal surfaces. On C4n1, COF in dry environment is not significantly different from that in ambient environment, though the former is slightly higher than the later. In contrast, on PEAn1, higher RH results in higher COF. The difference might be related to the hydrophobicity of the spacer molecules, the moisture-induced packing of the organic ligands on the surfaces, and the non-monotonic dependence of COF on the amount of water molecules at the tip-sample interface.

Table 1 Final resulted COF of HOIP samples under different environment condition.

HOIP Sample	Environment Condition	Resulted COF
C4n1	Ambient	0.225 ± 0.112
	Controlled	0.239 ± 0.066
PEAn1	Ambient	0.092 ± 0.041
	Controlled	0.072 ± 0.039

Our results suggest the PEA-based 2D HOIPs have low COFs than BA-based 2D HOIPs. Lower COFs together with higher hardness indicates these PEA-based 2D HOIPs should exhibit better resistance to mechanical wear than BA-based 2D HOIPs, and thus can give longer lifetime in TENG applications. Note that, because of the π −conjugated electrons in the phenyl groups, PEA-based 2D HOIPs also exhibits much better out-of-plane conductivity than their BA-counterparts, which can significantly facilitate the charge collection in TENG devices. Our results suggest that PEA is superior to BA for 2D HOIPs-based TENG. However, caution must be taken about the humidity of the application environment, as relatively high humidity can result in a high COF in PEA-based 2D HOIPs and thus more wear.

Future Scopes

In this work, I have assumed that 2D HOIPs shows linear friction relationship with normal load, with respect to linear friction response of similar end functional group SAMs work reported. But from Figure 12 and similar results, the response might not be linear

due to presence of adhesive force of organic ligands with the tip. The possibility of non-linear friction can be found by performing hysteresis curve for friction response with respect to normal load or by conducting ‘Stribeck curve’ for the friction response of 2D HOIPs. We can also determine non-linearity by changing the scanning parameters and see the affected changes in friction response. This study can help us determine the effect of normal load on friction behavior of 2D HOIPs.

2D structure enables a vast parameter space to engineer the properties of HOIPs. Within the two widely used spacer molecule families, *i.e.,* acene alkylamine and linear-alkylamine, how the size of the spacer molecules, *i.e.,* the linear alkyl chain length or the size of the fused benzine rings, will affect the friction behavior of the 2D HOIPs needs to be further investigated. Furthermore, the inorganic lead-halide framework might affect the packing and interfacial interactions between these organic spacer molecules. The effects of the key parameters of the inorganic octahedral framework, including the n number and the halide ion species, on the friction properties of 2D HOIPs requires more study. These additional researches can provide a comprehensive picture of the structure-frictional-properties of the 2D HOIPs and provide tribological insights into device designs where the frictional properties matter.

Our results suggest the humidity has an impact on the frictional properties of the 2D HOIP crystals. A better of the humidity range with finer humidity steps can unveil the detailed trend of the frictional properties of 2D HOIPs on the humidity for different compositions, which would generate indispensable insights into the mechanism of the humidity influence on the frictional properties of 2D HOIPs and thus guide the

engineering of 2D HOIPs' composition to achieve desired level of friction for applications at various humidity environments. Besides humidity, temperature is another common stressor that can alter the structure of the 2D HOIPs, including the octahedral tilting and distortion and the order-disorder transition of the organic spacer molecules, which could modulate the frictional properties of 2D HOIPs and calls for further examinations. Finally, polycrystalline 2D HOIP films are widely used in device applications. In this case, the grain structure and the orientation of the 2D basal planes in the film (i.e., horizontal or vertical) can greatly affect the tribological properties of 2D HOIP films, which need systematic investigation.

REFERENCES

1. Green, M.A., et al., *Optical properties of photovoltaic organic–inorganic lead halide perovskites.* The journal of physical chemistry letters, 2015. **6**(23): p. 4774-4785.
2. Chen, Y., et al., *Extended carrier lifetimes and diffusion in hybrid perovskites revealed by Hall effect and photoconductivity measurements.* Nature communications, 2016. **7**(1): p. 1-9.
3. Miyata, A., et al., *Direct measurement of the exciton binding energy and effective masses for charge carriers in organic–inorganic tri-halide perovskites.* Nature Physics, 2015. **11**(7): p. 582-587.
4. Shi, D., et al., *Low trap-state density and long carrier diffusion in organolead trihalide perovskite single crystals.* Science, 2015. **347**(6221): p. 519-522.
5. Chen, J., et al., *Tin (IV)-tolerant vapor-phase growth and photophysical properties of aligned cesium tin halide perovskite (CsSnX3; X= Br, I) nanowires.* ACS Energy Letters, 2019. **4**(5): p. 1045-1052.
6. Lee, M.M., et al., *Efficient hybrid solar cells based on meso-superstructured organometal halide perovskites.* Science, 2012. **338**(6107): p. 643-647.
7. Liu, M., M.B. Johnston, and H.J. Snaith, *Efficient planar heterojunction perovskite solar cells by vapour deposition.* Nature, 2013. **501**(7467): p. 395-398.
8. Ji, L.-J., et al., *Mechanical properties of hybrid organic-inorganic perovskites.* Coordination Chemistry Reviews, 2019. **391**: p. 15-29.
9. Gao, H., et al., *Mechanical Properties of a 2D Lead-Halide Perovskite,(C6H5CH2NH3) 2PbCl4, by Nanoindentation and First-Principles Calculations.* The Journal of Physical Chemistry C, 2020. **124**(35): p. 19204-19211.
10. Tu, Q., et al., *Exploring the factors affecting the mechanical properties of 2D hybrid organic–inorganic perovskites.* ACS applied materials & interfaces, 2020. **12**(18): p. 20440-20447.
11. Shin, D.H., J.H. Heo, and S.H. Im, *Recent advances of flexible hybrid perovskite solar cells.* Journal of the Korean Physical Society, 2017. **71**(10): p. 593-607.
12. Ogletree, D., R.W. Carpick, and M. Salmeron, *Calibration of frictional forces in atomic force microscopy.* Review of Scientific Instruments, 1996. **67**(9): p. 3298-3306.
13. Wang, Y., et al., *The unique dielectricity of inorganic perovskites toward high-performance triboelectric nanogenerators.* Nano Energy, 2020. **69**: p. 104418.
14. Wang, M., et al., *Interfacial electric field enhanced charge density for robust triboelectric nanogenerators by tailoring metal/perovskite Schottky junction.* Nano Energy, 2020. **73**: p. 104747.
15. Wei, S., et al., *Flexible quasi-2D perovskite/IGZO phototransistors for ultrasensitive and broadband photodetection.* Advanced Materials, 2020. **32**(6): p. 1907527.

16. Su, L., et al., *High-performance organolead halide perovskite-based self-powered triboelectric photodetector.* ACS nano, 2015. **9**(11): p. 11310-11316.
17. GIOVANNI, D., *OPTICAL-SPIN DYNAMICS IN ORGANIC-INORGANIC HYBRID LEAD HALIDE PEROVSKITES.*
18. Yang, J. and T.L. Kelly, *Decomposition and cell failure mechanisms in lead halide perovskite solar cells.* Inorganic chemistry, 2017. **56**(1): p. 92-101.
19. Serrano-Lujan, L., et al., *Tin-and lead-based perovskite solar cells under scrutiny: an environmental perspective.* Advanced Energy Materials, 2015. **5**(20): p. 1501119.
20. Grancini, G. and M.K. Nazeeruddin, *Dimensional tailoring of hybrid perovskites for photovoltaics.* Nature Reviews Materials, 2019. **4**(1): p. 4-22.
21. Luo, S.-Q., et al., *Recent advances in controlling the crystallization of two-dimensional perovskites for optoelectronic device.* Frontiers of Physics, 2019. **14**(5): p. 1-17.
22. Kumar, A., et al., *Excitons in 2D perovskites for ultrafast terahertz photonic devices.* Science advances, 2020. **6**(8): p. eaax8821.
23. Vassilakopoulou, A., D. Papadatos, and I. Koutselas, *Room temperature light emitting diode based on 2D hybrid organic-inorganic low dimensional perovskite semiconductor.* Applied Materials Today, 2016. **5**: p. 128-133.
24. Sum, T.C. and N. Mathews, *Advancements in perovskite solar cells: photophysics behind the photovoltaics.* Energy & Environmental Science, 2014. **7**(8): p. 2518-2534.
25. Tiep, N.H., Z. Ku, and H.J. Fan, *Recent advances in improving the stability of perovskite solar cells.* Advanced Energy Materials, 2016. **6**(3): p. 1501420.
26. Dou, L., et al., *Atomically thin two-dimensional organic-inorganic hybrid perovskites.* Science, 2015. **349**(6255): p. 1518-1521.
27. Yin, J., et al., *Layer-dependent Rashba band splitting in 2D hybrid perovskites.* Chemistry of Materials, 2018. **30**(23): p. 8538-8545.
28. Goldschmidt, V.M., *The principles of distribution of chemical elements in minerals and rocks. The seventh Hugo Müller Lecture, delivered before the Chemical Society on March 17th, 1937.* Journal of the Chemical Society (Resumed), 1937: p. 655-673.
29. Saparov, B. and D.B. Mitzi, *Organic–Inorganic Perovskites: Structural Versatility for Functional Materials Design.* Chemical Reviews, 2016. **116**(7): p. 4558-4596.
30. Chen, Y., et al., *2D Ruddlesden–Popper perovskites for optoelectronics.* Advanced Materials, 2018. **30**(2): p. 1703487.
31. Mao, L., C.C. Stoumpos, and M.G. Kanatzidis, *Two-dimensional hybrid halide perovskites: principles and promises.* Journal of the American Chemical Society, 2018. **141**(3): p. 1171-1190.
32. Yu, J., M. Wang, and S. Lin, *Probing the Soft and Nanoductile Mechanical Nature of Single and Polycrystalline Organic–Inorganic Hybrid Perovskites for Flexible Functional Devices.* ACS Nano, 2016. **10**(12): p. 11044-11057.

33. Kim, D.B., J.W. Lee, and Y.S. Cho, *Anisotropic In Situ Strain-Engineered Halide Perovskites for High Mechanical Flexibility.* Advanced Functional Materials, 2021. **31**(4): p. 2007131.
34. Tu, Q., et al., *Stretching and breaking of ultrathin 2D hybrid organic–inorganic perovskites.* ACS nano, 2018. **12**(10): p. 10347-10354.
35. Osada, M. and T. Sasaki, *Nanoarchitectonics in dielectric/ferroelectric layered perovskites: from bulk 3D systems to 2D nanosheets.* Dalton Transactions, 2018. **47**(9): p. 2841-2851.
36. Li, Q., et al., *Atomic layer dependence of shear modulus in a two-dimensional single-crystal organic–inorganic hybrid perovskite.* The Journal of Physical Chemistry C, 2019. **123**(24): p. 15251-15257.
37. Feng, J., *Mechanical properties of hybrid organic-inorganic CH3NH3BX3 (B= Sn, Pb; X= Br, I) perovskites for solar cell absorbers.* Apl Materials, 2014. **2**(8): p. 081801.
38. Rakita, Y., et al., *Mechanical properties of APbX 3 (A= Cs or CH 3 NH 3; X= I or Br) perovskite single crystals.* Mrs Communications, 2015. **5**(4): p. 623-629.
39. Sun, S., et al., *Mechanical properties of organic–inorganic halide perovskites, CH 3 NH 3 PbX 3 (X= I, Br and Cl), by nanoindentation.* Journal of Materials Chemistry A, 2015. **3**(36): p. 18450-18455.
40. Reyes-Martinez, M.A., et al., *Time-Dependent Mechanical Response of APbX3 (A= Cs, CH3NH3; X= I, Br) Single Crystals.* Advanced Materials, 2017. **29**(24): p. 1606556.
41. Li, Z., et al., *The elastic and electromechanical properties of tetragonal BaTiO3 single crystals.* Journal of Applied Physics, 1991. **70**(12): p. 7327-7332.
42. Fett, T., D. Munz, and G. Thun, *Nonsymmetric deformation behavior of lead zirconate titanate determined in bending tests.* Journal of the American Ceramic Society, 1998. **81**(1): p. 269-272.
43. Shahraki, M.G., S. Ghorbanali, and H. Savaloni, *Influence of crystallographic orientation and diameter on piezoelectric constant and Young′ s modulus of BaTiO3 nanobelts.* Solid state communications, 2014. **196**: p. 40-45.
44. Hopcroft, M.A., W.D. Nix, and T.W. Kenny, *What is the Young's Modulus of Silicon?* Journal of microelectromechanical systems, 2010. **19**(2): p. 229-238.
45. McSkimin, H. and D. Thomas, *Elastic moduli of cadmium telluride.* Journal of Applied Physics, 1962. **33**(1): p. 56-59.
46. Berry, J., et al., *Hybrid organic–inorganic perovskites (HOIPs): opportunities and challenges.* Advanced Materials, 2015. **27**(35): p. 5102-5112.
47. Lin, Y.H., P. Pattanasattayavong, and T.D. Anthopoulos, *Metal-halide perovskite transistors for printed electronics: challenges and opportunities.* Advanced Materials, 2017. **29**(46): p. 1702838.
48. Huang, J., et al., *Understanding the physical properties of hybrid perovskites for photovoltaic applications.* Nature Reviews Materials, 2017. **2**(7): p. 1-19.
49. Tu, Q., et al., *Out-of-plane mechanical properties of 2D hybrid organic–inorganic perovskites by nanoindentation.* ACS applied materials & interfaces, 2018. **10**(26): p. 22167-22173.

50. Wilson, J.N., et al., *Dielectric and ferroic properties of metal halide perovskites.* APL Materials, 2019. **7**(1): p. 010901.
51. Ryu, H., et al., *High-performance triboelectric nanogenerators based on solid polymer electrolytes with asymmetric pairing of ions.* Advanced Energy Materials, 2017. **7**(17): p. 1700289.
52. Fan, F.R., W. Tang, and Z.L. Wang, *Flexible nanogenerators for energy harvesting and self-powered electronics.* Advanced Materials, 2016. **28**(22): p. 4283-4305.
53. Fan, F.-R., Z.-Q. Tian, and Z.L. Wang, *Flexible triboelectric generator.* Nano energy, 2012. **1**(2): p. 328-334.
54. Yang, Y., H. Zhang, and Z.L. Wang, *Direct-current triboelectric generator.* Advanced Functional Materials, 2014. **24**(24): p. 3745-3750.
55. Yang, Y., et al., *Human skin based triboelectric nanogenerators for harvesting biomechanical energy and as self-powered active tactile sensor system.* ACS nano, 2013. **7**(10): p. 9213-9222.
56. Zhao, K., et al., *Nanogenerator-based self-charging energy storage devices.* Nano-Micro Letters, 2019. **11**(1): p. 1-19.
57. Wen, X., et al., *Applicability of triboelectric generator over a wide range of temperature.* Nano Energy, 2014. **4**: p. 150-156.
58. Ding, R., M.C. Wong, and J. Hao, *Recent advances in hybrid perovskite nanogenerators.* EcoMat, 2020. **2**(4): p. e12057.
59. Rolston, N., et al., *Mechanical integrity of solution-processed perovskite solar cells.* Extreme Mechanics Letters, 2016. **9**: p. 353-358.
60. Cheacharoen, R., et al., *Design and understanding of encapsulated perovskite solar cells to withstand temperature cycling.* Energy & Environmental Science, 2018. **11**(1): p. 144-150.
61. Rolston, N., et al., *Effect of cation composition on the mechanical stability of perovskite solar cells.* Advanced Energy Materials, 2018. **8**(9): p. 1702116.
62. Bi, S., et al., *Layer-dependent anisotropic frictional behavior in two-dimensional monolayer hybrid perovskite/ITO layered heterojunctions.* Physical Chemistry Chemical Physics, 2019. **21**(5): p. 2540-2546.
63. Sung, I.-H. and D.-E. Kim, *Surface damage characteristics of self-assembled monolayers of alkanethiols on metal surfaces.* Tribology Letters, 2004. **17**(4): p. 835-844.
64. Lee, S., et al., *Structure, wettability, and frictional properties of phenyl-terminated self-assembled monolayers on gold.* Langmuir, 2001. **17**(23): p. 7364-7370.
65. Tian, F., et al., *Humidity and temperature effect on frictional properties of mica and alkylsilane monolayer self-assembled on mica.* Langmuir, 1999. **15**(1): p. 244-249.
66. Qian, L., F. Tian, and X. Xiao, *Tribological properties of self-assembled monolayers and their substrates under various humid environments.* Tribology Letters, 2003. **15**(3): p. 169-176.

67. Berman, D., et al., *Nanoscale friction properties of graphene and graphene oxide.* Diamond and Related Materials, 2015. **54**: p. 91-96.
68. Xiao, J., et al., *Anisotropic friction behaviour of highly oriented pyrolytic graphite.* Carbon, 2013. **65**: p. 53-62.
69. Serpini, E., et al., *Nanoscale frictional properties of ordered and disordered MoS2.* Tribology International, 2019. **136**: p. 67-74.
70. Zhao, X. and S.S. Perry, *The role of water in modifying friction within MoS2 sliding interfaces.* ACS applied materials & interfaces, 2010. **2**(5): p. 1444-1448.
71. Bennewitz, R., *Friction force microscopy.* Fundamentals of Friction and Wear on the Nanoscale, 2015: p. 3-16.
72. Bhushan, B. and S. Sundararajan, *Micro/nanoscale friction and wear mechanisms of thin films using atomic force and friction force microscopy.* Acta Materialia, 1998. **46**(11): p. 3793-3804.
73. Gnecco, E., et al., *Friction and wear on the atomic scale.* Wear, 2003. **254**(9): p. 859-862.
74. Corporation, B. *How LFM works*. 2011; Available from: https://www.nanophys.kth.se/nanolab/afm/icon/bruker-help/Content/LFM/How%20LFM%20Works.htm.
75. Palacio, M.L. and B. Bhushan, *Normal and lateral force calibration techniques for AFM cantilevers.* Critical Reviews in Solid State and Materials Sciences, 2010. **35**(2): p. 73-104.